J. Fluid Mech. (2002), *vol.* 450, *pp.* 235–258. © 2002 Cambridge University Press
DOI: 10.1017/S0022112001006395 Printed in the United Kingdom

Instability of an annular jet surrounded by a viscous gas in a pipe

By J. N. CHEN AND S. P. LIN

Department of Mechanical and Aeronautical Engineering, Clarkson University, Potsdam, NY 13699-5725, USA

(Received 20 December 2000 and in revised form 22 June 2001)

The onset of instability in a liquid annular jet enclosing another fluid, and surrounded by a gas in a pipe is analysed by use of a spectra-collocation method. The dynamic responses to the variation of different flow parameters are elucidated by use of numerical results. Two linearly independent convectively unstable interfacial modes of disturbances are found. In general, the para-sinuous mode has a larger amplification rate than the para-varicose mode. It is shown that to initiate encapsulation of core fluid with a uniform shell fluid, the growth of the para-sinuous mode must be promoted and the para-varicose mode must be suppressed. Suppression of the para-varicose mode in a finite range of wavenumbers is possible by varying the flow parameters. The effects of ten relevant parameters on instability are discussed. In certain parameter space, the annular jet becomes absolutely unstable with respect to the sinuous mode. The transition Weber number below which the flow is absolutely unstable and above which the flow is convectively unstable is found as a function of the Reynolds number when the rest of flow parameters are given. A successful encapsulation of core fluid with a uniform shell fluid is possible if the process is carried out outside of the parameter space of absolute instability, and if an external forcing is introduced at a frequency within a band in which the para-varicose mode is stable but the para-sinuous mode is convectively unstable.

1. Introduction

Annular jets are encountered in many industrial processes. Their stability has been studied in the contexts of ink-jet printing (Hertz & Hermanrud 1983; Sanz & Meseguer 1985), encapsulation (Kendall 1986; Lee & Wang 1989), gas absorption (Baird & Davidson 1962), and atomization (Crapper, Dombowski & Pyott 1975; Lee & Chen 1991; Shen & Li 1996). Shen & Li analysed the spatio-temporal instability of an annular liquid jet surrounded by an inviscid gas. Hu & Joseph (1989) investigated the temporal instability of a three-layered liquid core–annular flow. The annular jet instability is also of considerable theoretical interest, since it includes many other flow instabilities as special cases (Meyer & Weihs 1987). Moreover, it serves to establish knowledge of the fluid physics of flows with two distinctive curved fluid–fluid interfaces subjected to different shear forces, capillary forces, and inertial forces under variable gravitational conditions.

The existing theoretical analyses of the present problem either neglect the viscosities of the fluid surrounding the annulus or approximate the basic flows which do not satisfy the governing equations exactly. Consequently, it is difficult to ascertain which part of the results extracted from the theory is attributable to the approximation and

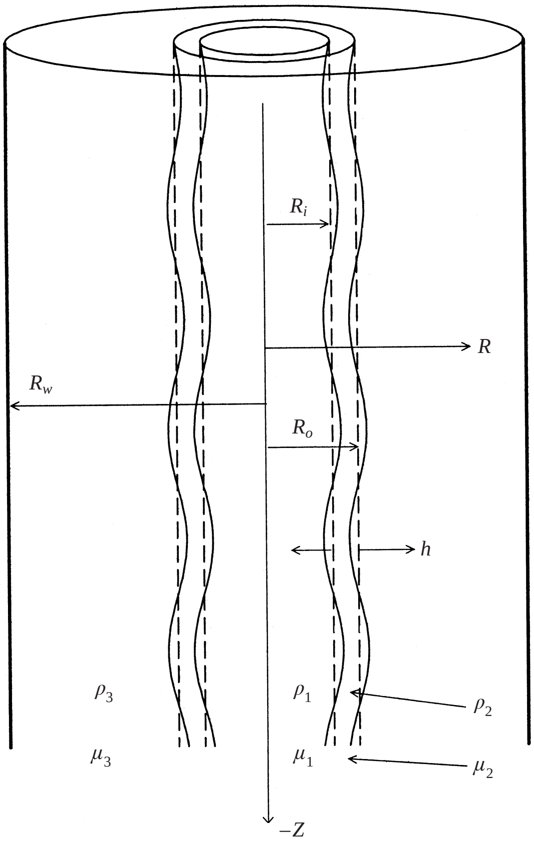

FIGURE 1. Definition sketch.

which part of the results is genuinely physical. For example, the effects of gravity, gas viscosity, and the difference in surface tension of the two interfaces are neglected in the work of Shen & Li (1996). They found that the amplification rate increases with the gas to liquid density ratio. However, this finding may not reflect a genuine effect of densities, since density and dynamic viscosity are coupled. The latter is neglected in their work. It turns out that when the gas viscosity is taken into account, the opposite of their conclusion on the density effect is true, except when the surface tension force is very small compared with the inertial force. Moreover, the existing theories cannot produce precisely the onset of absolute instability which must be avoided for a successful operation of encapsulation processes. To overcome this difficulty and to ascertain the true physical effects of each of the ten flow parameters involved, we have obtained a basic flow representing a liquid annular jet which satisfies the governing equation exactly. The stability analysis of this basic flow with respect to temporal as well as spatio-temporal disturbances are formulated in § 2. A spectral collocation method which is described in § 3 is then used to obtain the numerical results. The numerical results are then used in § 4 to elucidate the effects of all relevant flow parameters. The practical implications of the finding are discussed in § 5.

2. Formulation

Consider the flow of a liquid in an annulus enclosing a gas, which is surrounded by another gas inside a circular pipe of radius R_w as shown in figure 1. The axis of the pipe is aligned with the direction of the acceleration due to gravity $\boldsymbol{g}$. Both gases and the liquid are Newtonian. The governing equations of motion of the fluids, assumed to be incompressible are

$$\partial_t \boldsymbol{V}_j + \boldsymbol{V}_j \cdot \nabla \boldsymbol{V}_j = -\frac{1}{\rho_j} \nabla \cdot \boldsymbol{\sigma}_j, \tag{1}$$

$$\nabla \cdot \boldsymbol{V}_j = 0 \quad (j = 1, 2, 3), \tag{2}$$

where $j = 1$, 2 and 3 designate the inner gas, the liquid, and the outer gas, respectively, t is time, $\boldsymbol{V}$ is the velocity, ρ is the density and $\boldsymbol{\sigma}$ is the stress tensor. For Newtonian fluids

$$\boldsymbol{\sigma}_j = -P\boldsymbol{I} + \mu_j[\nabla \boldsymbol{V}_j) + (\nabla \boldsymbol{V}_j)^T],$$

where P is the pressure, $\boldsymbol{I}$ is the identity matrix and μ is the dynamic viscosity.

The corresponding boundary conditions are the no-slip conditions at the pipe inner wall, i.e.

$$\boldsymbol{V}_3 = 0 \quad \text{at} \quad R = R_w, \tag{3}$$

where R is the radial distance in the cylindrical coordinates (R, θ, Z); the continuity of the velocity at each fluid–fluid interface, i.e.

$$\boldsymbol{V}_1 = \boldsymbol{V}_2 \quad \text{at} \quad R = R_i, \tag{4}$$

$$\boldsymbol{V}_2 = \boldsymbol{V}_3 \quad \text{at} \quad R = R_o, \tag{5}$$

where R_i and R_o are, respectively, the inner radius and outer radius of the annulus; the kinematic conditions at the interface, i.e.

$$U_{1,3} = (\partial_t + \boldsymbol{V}_{1,3} \cdot \nabla)R \quad \text{at} \quad R = R_i \quad \text{or} \quad R_o, \tag{6}$$

where U is the radial component of the velocity, and the subscript 1, followed by 3 after a comma designates either fluid 1 or fluid 3; the dynamic boundary condition at the fluid–fluid interfaces,

$$(\boldsymbol{\sigma}_2 - \boldsymbol{\sigma}_1) \cdot \boldsymbol{n}_i - \boldsymbol{n}_i \cdot S_i \nabla \cdot \boldsymbol{n}_i = 0 \quad \text{at} \quad R = R_i, \tag{7}$$

$$(\boldsymbol{\sigma}_3 - \boldsymbol{\sigma}_2) \cdot \boldsymbol{n}_o - \boldsymbol{n}_o \cdot S_o \nabla \cdot \boldsymbol{n}_o = 0 \quad \text{at} \quad R = R_o, \tag{8}$$

where S_i and S_o are, respectively, the surface tensions of the inner and the outer interfaces, and $\boldsymbol{n}_i$ and $\boldsymbol{n}_o$ are, respectively, the unit normal vectors of the interfaces defined by

$$F_i = R - R_i = 0 \quad \text{and} \quad F_o = R - R_o = 0.$$

The unit normal vectors at the two interfaces are defined to be positive if they point in a positive radial direction. Thus,

$$(\boldsymbol{n}_i, \boldsymbol{n}_o) = (\nabla F / |\nabla F_i|,\ \nabla F_o / |\nabla F_o|). \tag{9}$$

We seek an axisymmetric non-swirling steady constant radius annular basic flow which satisfies exactly the above governing equations and their boundary conditions. For such a flow, the radial and azimuthal velocity components must vanish, and the pressure differences across each fluid–fluid interface must balance exactly the surface tension forces associated with the two different radii at any axial location at all times. Thus, the axial dynamic pressure gradient in each fluid must be constant but of different value, because of the different hydrostatic pressure experienced by each fluid. It is easily verified that the governing equations (1) and (2) are reduced to

$$\frac{N_j}{Re}\frac{1}{r}\,\partial_r(r\,\partial_r\bar{w}_j) = -K_j, \tag{10}$$

$$K_j = \left(-\frac{1}{Q_j}\,\partial_z\bar{p}_j - Fr^{-1}\right),$$

where r and z are the radial and axial distances normalized with the characteristic length H, and $\bar{w}$ is the axial velocity normalized with a reference velocity W_m. Both H and W_m are yet to be chosen. $\bar{p} = P/\rho_2 W_m^2$ is the dimensionless pressure, Re, Fr, N_j and Q_j are, respectively, the Reynolds number, the Froude number, the kinematic viscosity ratio and the density ratio defined by

$$Re = \frac{W_m H}{\nu_2}, \quad Fr = \frac{W_m^2}{gH}, \quad N_j = \frac{\nu_j}{\nu_2}, \quad Q_j = \frac{\rho_j}{\rho_2}.$$

ν being the kinematic viscosity.

Integration of (10) yields

$$\bar{w}_j = -\frac{K_j}{4N_j}Re\,r^2 + C_{j1}\ln r + C_{j2}, \tag{11}$$

where C_{j1} and C_{j2} are integration constants determined by the boundary conditions to be

$$\begin{aligned}
C_{11} &= 0,\\
C_{21} &= (1-Q_1)Re\,Fr^{-1}\,r_i^2/2,\\
C_{31} &= (Q_3-1)Re\,Fr^{-1}\,r_o^2/(2Q_3N_3) + C_{21}/(Q_3N_3),\\
C_{22} &= (K_2-K_3/N_3)Re\,r_o^2/4 + (C_{31}-C_{21})\ln r_o + C_{32},\\
C_{12} &= (K_2-K_1/N_1)Re\,r_i^2/4 + C_{21}\ln r_i + C_{22},\\
C_{32} &= K_3\,Re\,r_w^2/(4N_3) - C_{31}\ln r_w,\\
K_1 &= [K_2+(1-Q_1)F_r^{-1}]/Q_1,\\
K_3 &= [K_2+(1-Q_3)F_r^{-1}]/Q_3,
\end{aligned}$$

where K_2 depends on the choice of the length scale H and the velocity reference W_m. It is found that for better numerical accuracy, H and W_m should be chosen, respectively, as the liquid shell thickness h, and the liquid velocity at $r = \frac{1}{2}(r_i + r_o)$. For this choice of normalization,

$$\begin{aligned}
K_2 &= \{-4 + Re\,F_r^{-1}\,A_1 - 4[C_{21}\ln((r_i+r_o)/2) + A_2]\}/Re[-(r_i+r_o)^2/4 + A_3],\\
A_1 &= (Q_3^{-1}-1)(r_o^2+r_w^2)/N_3,\\
A_2 &= (C_{31}-C_{21})\ln r_o - C_{31}\ln r_w,\\
A_3 &= (1-Q_3^{-1}\,N_3^{-1})r_o^2 + r_w^2/Q_3N_3.
\end{aligned}$$

On the other hand, it is more expedient to normalize the length and velocity, respectively, with the core gas radius and the core gas velocity along the pipe axis, for a direct comparison with the known results of the axisymmetric Poiseuille flow and the simple liquid jet. For this latter normalization (scaling I),

$$K_2 = \{-4 + Re\,F_r^{-1}[(Q_1^{-1}-1)r_i^2/N_1 + A_1] - 4(C_{21}\ln r_i + A_2)\}/Re[(1-Q_1^{-1}N_1^{-1})r_i^2 + A_3].$$

A representative basic flow velocity distribution is given in figure 2.

To investigate the onset of instability in this basic flow we introduce disturbances to

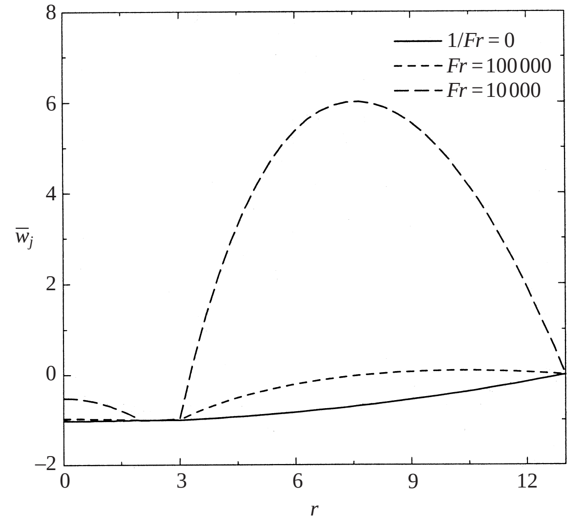

FIGURE 2. The effects of Froude number on the basic velocity profile, $Re = 1000$, $Q_1 = Q_3 = 0.0013$, $\bar{N}_1 = 0.018$, $\bar{N}_3 = 0.18$, $r_t = 2$, $r_w = 13$.

the basic flow and analyse the spatio-temporal behaviour of the disturbance. Related experiments (Kendall 1986) show that the consequence of instability is the formation of axisymmetric compound drops, unless the Reynolds number is so high that non-axisymmetric sprays may result (Lee & Chen 1991). We focus here on the formation of axisymmetric compound drops, and assume the disturbance to be axisymmetric. Hence, we write

$$(w_j, u_j, p_j) = (\bar{w}_j + w_j,\ u_j',\ \bar{p}_j + p_j'), \tag{12}$$

where prime quantities represent perturbations. The governing equations for the onset of instability are obtained by substituting (12) into (1) and (2) and keeping only the linear terms. Equation (2) allows us to relate the velocity perturbation to the Stokes stream function ψ, i.e.

$$(u_j', w_j') = \frac{1}{r}(\partial_z, -\partial_r)\psi.$$

The curl of (1) written in terms of ψ is (cf. Drazin & Reid 1985),

$$\left(\partial_\tau - \frac{N_j}{Re}E^2\right)E^2\psi_j + \bar{w}_j E^2\,\partial_z\psi_j - r\,\partial_r\left(\frac{1}{r}\partial_r\bar{w}_j\right)\partial_z\psi_j = 0, \tag{13}$$

where τ is the dimensionless time $\tau = t/(W_m/h)$, and

$$E^2 = \partial_{rr} - \frac{1}{r}\partial_r + \partial_{zz}.$$

Although the pressure does not appear in the governing equation (13), it remains in the dynamic boundary conditions at the interfaces which are displaced by amounts (η_i, η_o) where the subscripts i and o again stand for the inner and outer interfaces, respectively. We seek the normal mode solution of the governing differential system, and express the perturbation as

$$[\psi_j, p_j, \eta_i, \eta_o] = [\phi_j(r), \zeta_j(r), \xi_i, \xi_o]\exp[\mathrm{i}kz + \omega\tau],$$

where $k = k_r + \mathrm{i}k_i$ and $\omega = \omega_r + \mathrm{i}\omega_i$ are respectively the complex wavenumber and the complex wave frequency of the disturbance. The real part of the wavenumber k_r is related to the wavelength λ by $k_r = 2\pi h/\lambda$. The corresponding frequency is ω_i. The terms ω_r and k_i give, respectively, the temporal and spatial growth rates. In terms of the perturbation amplitude functions, (13) can be written as

$$\left(\omega - \frac{N_j}{Re}\mathrm{E}_1^2\right)\mathrm{E}_1^2\phi_j + \mathrm{i}k\bar{w}_j\mathrm{E}_1^2\phi_j - \mathrm{i}kr\mathrm{D}\left(\frac{1}{r}\mathrm{D}\bar{w}_j\right)\phi_j = 0, \tag{14}$$

$$\mathrm{E}_1^2 = \frac{\mathrm{d}^2}{\mathrm{d}r^2} - \frac{1}{r}\frac{\mathrm{d}}{\mathrm{d}r} - k^2, \quad \mathrm{D} = \frac{\mathrm{d}}{\mathrm{d}r}.$$

The boundary conditions corresponding to (3)–(8) written out in cylindrical components in the same order are

$$\phi_3(r_w) = 0, \tag{15}$$

$$\mathrm{D}\phi_3(r_w) = 0, \tag{16}$$

$$\phi_{1,3}(r_{i,o}) = \phi_2(r_{i,o}), \tag{17}$$

$$\frac{1}{r_{i,o}}[\mathrm{D}\phi_{1,3}(r_{i,o}) - \mathrm{D}\phi_2(r_{i,o})] = [\mathrm{D}\bar{w}_{1,3}(r_{i,o}) - \mathrm{D}\bar{w}_2(r_{i,o})]\xi_{i,o}, \tag{18}$$

$$\frac{\mathrm{i}k}{r_{io}}\phi_{1,3}(r_{i,o}) = [\omega + \bar{w}_{1,3}(r_{i,o})]\xi_{i,o}, \tag{19}$$

$$Q_{1,3}N_{1,3}\mathrm{E}^{-2}\phi_{1,3}(r_{i,o}) - \mathrm{E}^{-2}\phi_2(r_{i,o}) = \xi_{i,o}[Q_{1,3}N_{1,3}\mathrm{D}^2\bar{w}_{1,3}(r_i, r_o) - \mathrm{D}^2\bar{w}_2(r_{i,o})], \tag{20}$$

$$\begin{aligned} &Q_{1,3}[\omega + \mathrm{i}k\bar{w}_{1,3}(r_{i,o})]\mathrm{E}\phi_{1,3}(r_{i,o}) - [\omega + \mathrm{i}k\bar{w}(r_{i,o})]\mathrm{D}\phi_2(r_{i,o}) \\ &-\mathrm{i}k[\mathrm{D}\bar{w}_{1,3}(r_{i,o})\phi_{1,3}(r_{i,o}) - \mathrm{D}\bar{w}_2(r_{i,o}) - \phi_2(r_{i,o})] \\ &+\frac{1}{Re}\left\{\left[\mathrm{L}\phi_2(\bar{r}_{i,o}) - 2k^2\left(\mathrm{D}\phi_2(r_{i,o}) - \frac{1}{r_{i,o}}\phi_2(r_{i,o})\right)\right]\right. \\ &\left.-Q_{1,3}N_{1,3}\left[\mathrm{L}\phi_{1,3}(r_{i,o}) - 2k^2\mathrm{D}\phi_{1,3}\left(r_{i,o} - \frac{1}{r_{i,o}}\phi_{i,o}(r_{i,o})\right)\right]\right\} \\ &+\mathrm{i}kW\,e_{i,o}^{-1}\left(\frac{1}{r_{i,o}} - k^2 r_{i,o}\right)\xi_{i,o} = 0, \end{aligned} \tag{21}$$

where $r = R/h$, and its subscripts retain the same designations as its dimensional counterparts. The term $r_{i,o}$ appearing in the argument of a function signifies that the function is to be evaluated at $r = r_i$ or $r = r_o$ depending on whether (20) is to be evaluated at the inner or outer interface, and

$$\mathrm{D}^2 = \frac{\mathrm{d}^2}{\mathrm{d}r^2}, \quad \mathrm{E}^{-2} = \frac{\mathrm{d}^2}{\mathrm{d}r^2} - \frac{1}{r}\frac{\mathrm{d}}{\mathrm{d}r} + k^2,$$

$$\mathrm{L} = \frac{\mathrm{d}^3}{\mathrm{d}r^3} - \frac{1}{r}\frac{\mathrm{d}^2}{\mathrm{d}r^2} - \left(\frac{1}{r^2} - k^2\right)\frac{\mathrm{d}}{\mathrm{d}r},$$

$$We_{i,o} = \rho_{1,3}W_m^2 h/S_{i,o}.$$

$We_{i,o}$ is the Weber number associated with the inner or the outer interfaces. Equations (15) and (16) are the no-slip conditions at the pipe wall. Equations (17) and (18) are, respectively, the continuity of the radial and tangential components of the velocity at the interfaces. Equation (19) is the interfacial kinematic condition, (20) and (21) are, respectively, the tangential and normal component of the dynamic boundary condition. Moreover, we shall demand that the solution is bounded along the cylindrical axis, i.e.

$$\phi_3(0) = \mathrm{D}\phi_3(0) = 0. \tag{22}$$

3. Numerical solution

First, the flow domain of each fluid is mapped into a strip of thickness 2 by use of the following linear transformations

$$y_j = a_j r + b_j, \tag{23}$$

where

$$\begin{gathered} a_1 = 2/r_i, \quad b_1 = -1, \\ a_2 = \frac{2}{r_i - r_0}, \quad b_2 = -\frac{r_i + r_o}{r_i - r_0}, \\ a_3 = \frac{2}{r_w - r_o}, \quad b_3 = -\frac{r_w + r_o}{r_w - r_o}. \end{gathered}$$

Hence,

$$\begin{gathered} r \in [0, r_i] \longrightarrow y_1 \in [-1, 1], \\ r \in [r_i, r_o] \longrightarrow y_2 \in [1, -1], \\ r \in [r_0, r_w] \longrightarrow y_3 \in [-1, 1], \end{gathered}$$

Then we write ϕ_j as the finite sum of a convergent series as (Boyd 1989),

$$\phi_j(y_j) = \sum_{n=0}^{M_j} h_{jn}(y_j)\phi_j(y_{jn}), \tag{24}$$

where y_{jn} is the Gauss–Lobatto collocation point given by

$$y_{jn} = \cos\left(\frac{\pi n}{M_j}\right),$$

and h_{jn} is the Lagrange cardinal function

$$h_{jn}(y_j) = \frac{(-1)^{n+1}(1 - y_j^2)}{C_n M_j^2 (y_j - y_{jn})} \frac{\mathrm{d}}{\mathrm{d}y} T_{M_j}(y_j), \tag{25}$$

$$C_0 = C_{M_j} = 2, \quad C_n = 1 \quad \text{for} \quad 1 \leqslant n \leqslant M_j - 1,$$

where $T_{M_j}(y_j)$ is the M_jth order Chebyshev polynomial

$$T_{M_j}(y) = \cos(M_j \cos^{-1} y) \quad -1 \leqslant y \leqslant 1.$$

Substitution of (24) into (14) and evaluating the resulting equation at $M_j - 4$ collocation points we have $M_1 + M_2 + M_3 - 12$ equations. We also have to satisfy the 17 equations from (15) to (22). Thus, we have a system of $M_1 + M_2 + M_3 + 5 = N$ equations

$$\boldsymbol{Ax} = \omega \boldsymbol{Bx} \tag{26}$$

in the same number of unknowns

$$\boldsymbol{x} = [(\phi_{10}, \ldots, \phi_{1M_1}),\ (\phi_{20}, \ldots, \phi_{2M_2}),\ (\phi_{30}, \ldots, \phi_{3M_3}),\ \xi_i,\ \xi_o].$$

The expressions of the $N \times N$ matrices $\boldsymbol{A}$ and $\boldsymbol{B}$ are given in the Appendix.

There are 10 flow parameters (Re, Fr, We_i, We_o, Q_1, Q_3, $\bar{N}_1$, $\bar{N}_3$, r_i, r_w), where $\bar{N}_1 = Q_1N_1$ and $\bar{N}_3 = Q_3N_3$. Note that $r_o = r_i + 1$. The annular liquid shell possesses two interfaces. Thus, it has two degrees of freedom, and the linear differential system possesses two independent interfacial modes of solution. Unlike a two-dimensional plane liquid sheet, the two modes are not exactly in phase or 180° out of phase, since the two interfaces are not exactly symmetrical with respect to the midsection of the annular sheet. However, they may be almost symmetrical if the curvature difference is small. Hence, we call the mode which displaces the two interfaces almost in phase the para-sinuous mode, and the mode which displaces the two interfaces 180° out of phase the para-varicose mode; or sinuous and varicose modes for simplicity. For purely temporal disturbances k is real, and if it is given together with the complete set of the flow parameters, then the complex wave frequency ω can be solved from (26) as the eigenvalue. The IMSL library routine GVLCG has been used to obtain ω. We characterize the spatial–temporal disturbances of a given wavenunber k_r for a given set of flow parameters with the spatial amplification curves $\omega_r = 0$. There are at least two such curves for a given set of flow parameters, in the case of convective instability. One corresponds to the sinuous mode and the other to the varicose mode. For each mode, we start with an initial guess of k_i for a given k_r, then solve for ω_r and ω_i using the IMSL routine GVCCG. If $\omega_r = 0$, the guess was perfect, if $\omega_r \neq 0$, we find k_i by use of the Newton iteration method with a reduced value of $|\omega_r|$. With the new k_i and the original k_r we update (ω_r, ω_i) by use of the IMSL routine GVCCG. We repeat this procedure until the IMSL routine gives $\omega_r = 0$. This iterative scheme requires a very close initial guess of k_i for convergence to the amplification curve $\omega_r = 0$. The close initial guess of k_i is achieved as follows. First, we seek the downstream-propagating convectively unstable branches. We start our search with a negative k_i in the (k_r, k_i)-plane. The image of the k with negative k_i should be a ω with positive ω_r. Then, the causality condition that the disturbance vanishes as $t \rightarrow -\infty$ in $z < 0$ is satisfied. With the given k, we obtain ω with subroutine GVLCG in the IMSL library. Two sets of (ω_r, ω_i) with $\omega_r > 0$ are found. We then increase k_i step by step until ω_r changes sign. The value of k_i which causes ω_r to change sign near to $\omega_r = 0$ is used as the initial guess for each mode. Once an accurate point on the amplification curve $\omega_r = 0$ is obtained with the iteration method described earlier, a sufficiently close point on the same curve can be obtained with the k_i on the neighbouring point without having to obtain the first guess of k_i as described. Similarly, the upstream branch $\omega_r = 0$ can be obtained by starting the initial guess of k_i with $k_i > 0$. When the downstream and upstream branches touch each other in the upper k-plane a saddle point of $\omega(k)$ is formed. The image of this saddle point in the upper ω-plane is a pinch point with $\omega_r > 0$. When a pinch point singularity appears, absolute instability results (Bers 1983; Briggs 1964).

The numbers of terms M_j retained in the series are systematically increased until the obtained eigenvalues remain the same up to the third decimal point. To test the possible syntax and computer program errors, the results for the special cases included in the present problem are checked against the known results of axisymmetric Poiseuille flow (Davey & Drazin 1969) and the cylindrical liquid jet in a concentric pipe (Lin & Chen 1998).

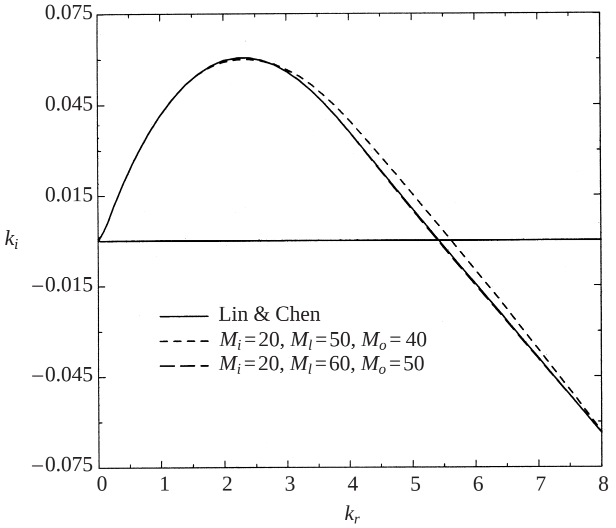

FIGURE 3. Amplification curve for a simple jet, $Re = 1000$, $1/Fr = 0.0001$, $We_i = 4761.9$, $We_0 = 0.0$, $Q_1^{-1} = 0.013$, $Q_3 = 1.0$, $\bar{N}_1^{-1} = 0.019$, $\bar{N}_3 = 1.0$, $r_i = 1.0$, $r_o = 5$, $r_w = 10$. Scaling I is used in this calculation.

4. Results and discussion

The known results for a cylindrical liquid jet in a coaxial pipe can be recovered by changing the core gas to a liquid and changing the liquid shell to the same gas as the outer gas. For example, to recover the results in figure 3 of Lin & Chen (1998), we put $Q_3 = 1$, $Q_1^{-1} = 0.0013$, $\bar{N}_3 = 1$, $We_o^{-1} = 0$, $We_i^{-1} = 4761.9$, $\bar{N}_1^{-1} = 0.019$, $r_i = 1$, $r_o = 5$, $r_w = 10$, $Re = 1000$ and $Fr^{-1} = 0.0001$. Note that the definition of the Weber number here is the inverse of that in Lin & Chen. The solid curve in figure 3 shows the results of Lin & Chen, and the other two curves are obtained from the present program with two different sets of M_j. The figure also serves to show how the terms of the series expansion can be increased to improve the numerical accuracy. The known results for the axisymmetric Poiseuille flow can also be recovered by changing all three fluids to the same fluid. This can be achieved by putting $Fr^{-1} = 0$, $Q_1 = Q_3 = 1$, $\bar{N}_1 = \bar{N}_3 = 1$, and $We_i^{-1} = We_o^{-1} = 0$. To compare with the results of Davey & Drazin (1969) we put $r_i = 1$, $r_o = 1.5$, $r_w = 2$, $k_r = 0.5$, $k_i = 0$ and $Re = 2500$. Note that while Davey & Drazin used the pipe radius, we use r_i to normalize the distance. Thus, $Re = 2500$ and $k_r = 0.5$ in figure 4 correspond to their value of 5000 and 1, respectively. Davey & Drazin used the Galerkin method to obtain the complex wave speed $c = c_r + \mathrm{i}c_i = \mathrm{i}\omega/k_r$. The comparison is excellent for the three upper branches. However, we have not found the lower two branches of Davey & Drazin for which a theoretical explanation is still lacking (Drazin & Reid 1985). Instead, we find the central branch $c_r = \frac{2}{3}$ to extend beyond their lower branches. Their two lower branches are most probably due to numerical inaccuracy associated with the Galerkin method. Figure 4 also shows how the number of terms M_j may be increased to improve the numerical accuracy. Sketches of sinuous and varicose modes are given in figure 5. For encapsulation applications, the varicose mode should be avoided, since the shell tends to pinch off at the location where the core is the thickest. This will lead to part of the core material being uncovered. Figure 6 gives the temporal growth rate ω_r and the spatial growth rate k_i as a function of k_r for the set of flow parameters shown in the caption. The values of Q_1, Q_3, $\bar{N}_1$

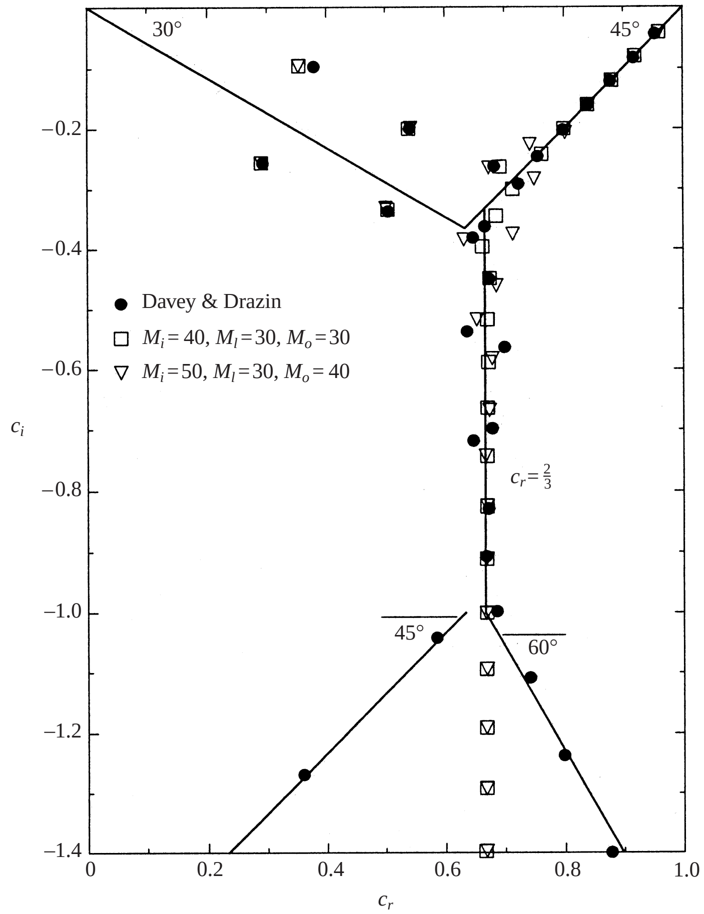

Figure 4. Values of c for $k_r = 0.5$, $k_i = 0$, $Re = 2500$, $1/Fr = 0.0$, $We_i^{-1} = 0.0$, $We_o^{-1} = 0.0$, $Q_1 = Q_3 = 1.0$, $\bar{N}_1 = \bar{N}_3 = 1.0$, $r_i = 1.0$, $r_o = 1.5$, $r_w = 2.0$. Scaling I is used in this calculation.

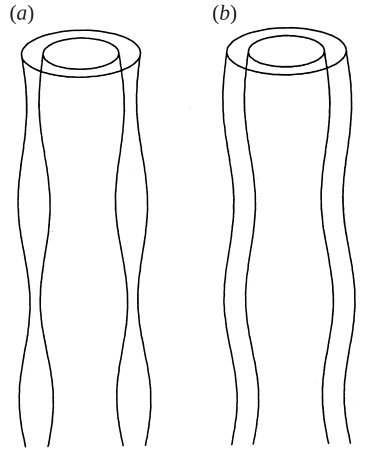

Figure 5. Schematic of (a) symmetric and (b) antisymmetric disturbances for annular liquid sheet.

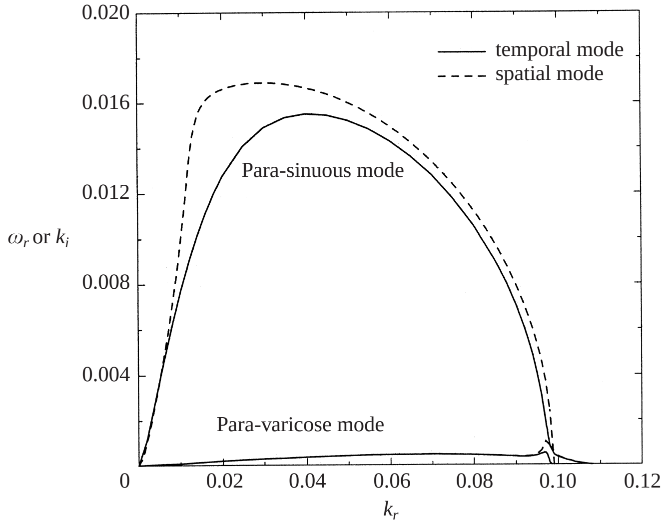

FIGURE 6. Temporal and spatial growth rates, $Re = 500$, $1/Fr = 0.0$, $We_i = We_o = 50$, $\bar{N}_1 = \bar{N}_3 = 0.018$, $Q_1 = Q_3 = 0.0013$, $r_i = 10$, $r_w = 21$.

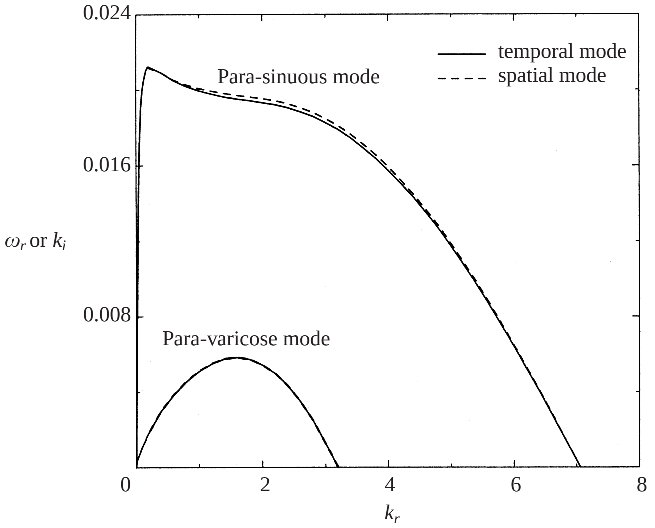

FIGURE 7. Temporal and spatial growth rates, $Re = 2000$, $Fr = 50\,000$, $We_i = We_o = 200\,000$, $\bar{N}_1 = \bar{N}_3 = 0.018$, $Q_1 = Q_3 = 0.0013$, $r_i = 10$, $r_w = 21$.

and $\bar{N}_3$ correspond to the case of a water annular jet enclosing air and surrounded by air at room conditions. The two curves are qualitatively the same except that the wavenumber corresponding to the maximum growth rates are smaller for the spatial disturbances for the sinuous mode. The two curves for the varicose mode are almost identical except near the cutoff wavenumber beyond which the amplification rates become negative. Figure 7 gives a similar set of two amplification curves for the same parameters as those given in figure 6, except that the Weber numbers are much larger. For relatively large Weber numbers, the temporal and spatial amplification curves fall almost on top of each other. A similar situation was encountered by Keller, Rubinow

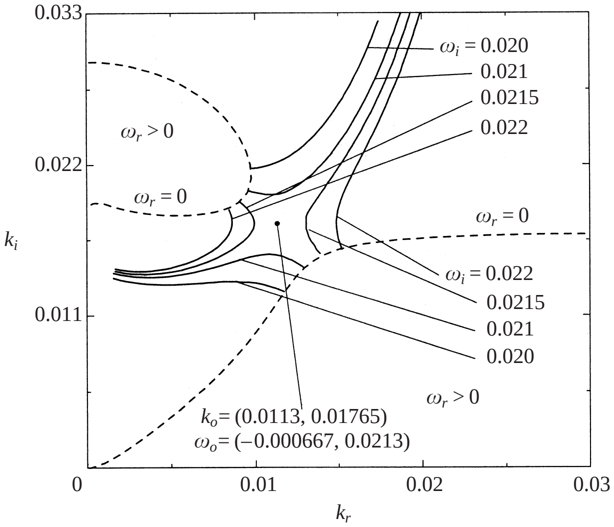

FIGURE 8. Convective instability, sinuous mode, $Re = 500$, $1/Fr = 0.0$, $We_i = We_o = 50$, $\bar{N}_1 = \bar{N}_3 = 0.018$, $Q_1 = Q_3 = 0.0013$, $r_i = 10$, $r_w = 21$.

& Tu (1973) in their analysis of a simple jet. The spatial amplification curves $\omega_r = 0$ in figures 6 and 7 can be approached from the lower half k-plane where $\omega_r > 0$ and $k_i < 0$ without encountering a pinch point singularity in the complex ω-plane. Therefore, the causality condition that initially no disturbances exist as $t \to -\infty$ and $z \to -\infty$ in the downstream region is satisfied. Moreover, ω_i increases with k_r along the spatial amplification curves. Hence, these curves represent downstream-propagating convectively unstable disturbances whose amplitude decays in time at a given point in space, but grows without bound with respect to an observer travelling with the disturbance group velocity (Briggs 1964; Bers 1983).

In some parameter space, the sinuous mode encounters in the k-plane a saddle-point singularity. An example of the emergence of a saddle point is illustrated in figures 8 and 9. There are two branches of the spatial amplification curves $\omega_r = 0$ in figure 8. The upper and lower branches can be reached from the upper and lower half k-planes, respectively. Along the upper branch $\mathrm{d}\omega_i/\mathrm{d}k_r < 0$, and along the lower branch $\mathrm{d}\omega_i/\mathrm{d}k_r > 0$. The lower branch represents the downstream-propagating convectively unstable disturbance. The upper branch represents the upstream-propagating evanescent waves. The saddle point in figure 8 does not prevent the deformation of the Fourier integral counters for superposing all Fourier components of either upstream- or downstream-propagating disturbances. As the Weber number is reduced from 50 given in the caption of figure 8 with the rest of the parameters fixed, the upper and the lower branches move toward each other, and at a critical Weber number they meet at a saddle point. The Weber number 45.0 in figure 9 slightly overshoots the critical Weber number. Figure 9 shows that when the critical Weber number is slightly exceeded, the upper and lower halves of the upper and the lower branch remain connected as they split off from the saddle point at the critical Weber number to form two new branches. The image of the saddle point in the k-plane is a pinch point singularity in the complex ω-plane with $\omega_r > 0$. Exact locations of the saddle points in the parameter space of ten dimensions is numerically tedious and expensive to obtain. The appearance of a saddle point signals the occurrence of absolute insta-

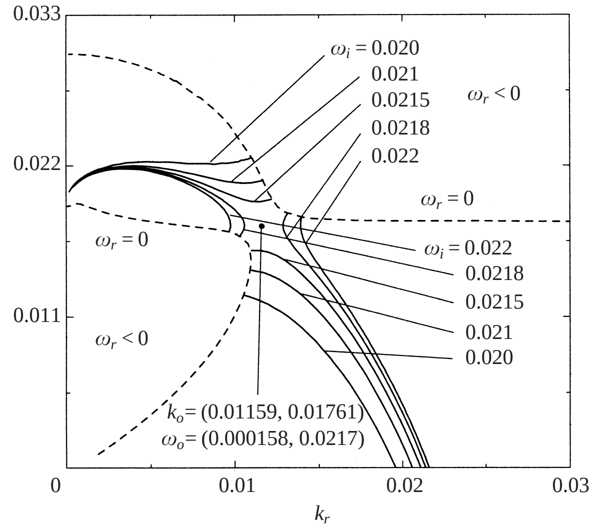

FIGURE 9. Absolute instability, sinuous mode, $Re = 500$, $1/Fr = 0.0$, $We_i = We_o = 45$, $\bar{N}_1 = \bar{N}_3 = 0.018$, $Q_1 = Q_3 = 0.0013$, $r_i = 10$, $r_w = 21$.

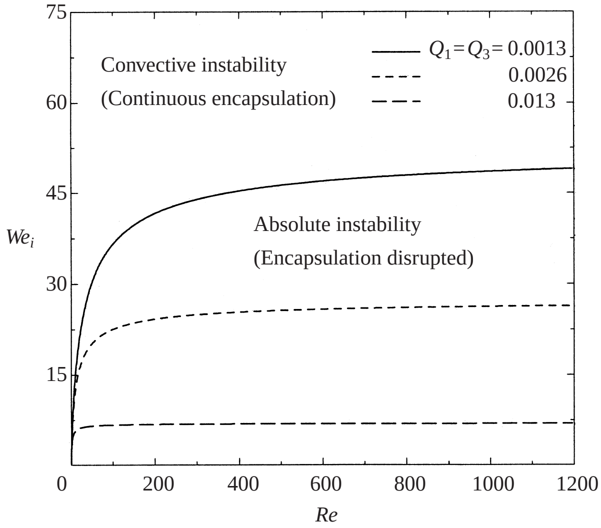

FIGURE 10. The critical Weber number for absolute instability, $1/Fr = 0.0$, $We_i = We_o$, $\bar{N}_1 = \bar{N}_3 = 0.018$, $r_i = 10$, $r_w = 21$.

bility in a flow in which a disturbance grows unbounded with time as it spreads in both the upstream and downstream directions.

Three curves, each with a given value of Q_1 and Q_3, which separate the parameter space into convective and absolute instability are given in figure 10. The fixed parameters are shown in the figure caption. Below each curve, the flow is absolutely unstable. Above each curve, the flow is convectively unstable. In the parameter space of absolute instability, the encapsulation by breaking an annular jet cannot be achieved, since the disturbance will propagate upstream to interrupt the process. However, in the convectively unstable regime, capsules can be formed if appropriate measures are taken, as will be explained shortly. Note that the region of absolute

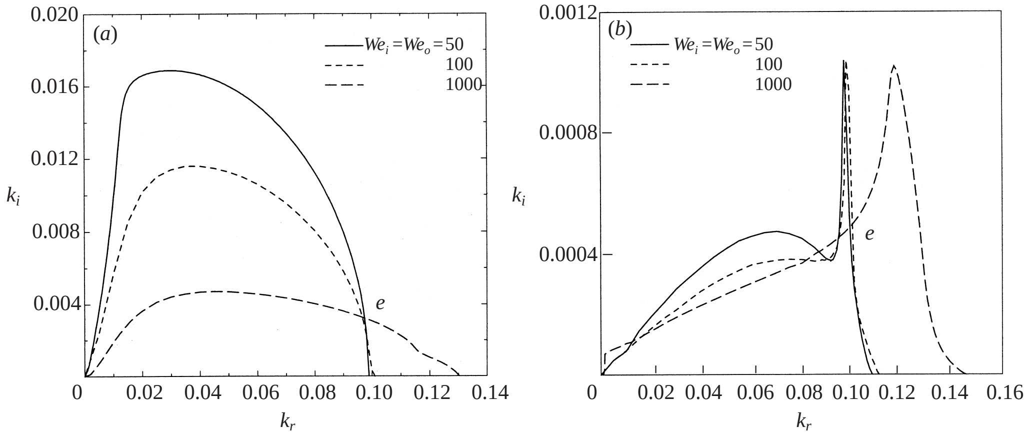

FIGURE 11. The effects of the Weber number on the spatial disturbance growth rate of convective instability $Re = 500$, $1/Fr = 0.0$, $\bar{N}_1 = \bar{N}_3 = 0.018$, $Q_1 = Q_3 = 0.0013$, $r_i = 10$, $r_w = 21$. (*a*) Para-sinuous mode. (*b*) Para-varicose mode.

instability, i.e. the region in which encapsulation is prohibited, increases with the increases in the density changes across the interfaces. This trend is opposite to that for the case of a simple jet in a pipe (O'Donnell, Chen & Lin 2001). The authors do not yet have a physical explanation for this difference.

Figures 11(*a*) and 11(*b*) show the effect of the Weber number variation on the rates of sinuous and varicose mode disturbances. For each Weber number set, the varicose mode has a slightly larger cutoff wavenumber above which the disturbance decays. Amplification curves of different Weber numbers intersect at point *e* for both modes. For sinuous disturbances with wave numbers smaller than that corresponding to point *e*, the amplification rate can be raised by decreasing the Weber number, by increasing the surface tension for example. Hence, the capillary force is destabilizing in this range of wavenumbers. The same conclusion applies to the varicose mode except in a very small wavenumber range. In this range as well as in the range of k_r greater than that corresponding to point *e* of both modes, the amplification curve for the larger Weber number is above that for the smaller one. Therefore, in these ranges the capillary force becomes stabilizing. Yet the jet is unstable in these ranges up to the cutoff wavenumber. Therefore, in these ranges the instability of both modes is caused by forces other than capillary force. These forces will be discussed later. Note that only in a very small range of wavenumber between the cutoff wavenumbers of the two modes for each Weber number in figure 11, does the varicose mode dominate over the sinuous mode. In almost all of the rest of the unstable wave spectrum, the amplification rate of the sinuous mode is one to two orders of magnitude larger than that of the varicose mode. However, a successful encapsulation is not easily achieved for the parameter specified in the figure, even if we impart an external forcing with frequencies corresponding to the wavenumbers in the range where the sinuous mode dominates over the varicose mode. This is because the varicose mode, however feeble, will still be excited together with the sinuous mode and this contaminates the encapsulation process.

The example given in figure 11 is for the case of zero gravity. The occurrence of the small range of wave spectrum, in which the undesirable varicose mode is dominant at finite gravity, is shown in figure 12. The para-sinuous and para-varicose mode amplification curves for $Fr = 1000$ intersect at point *e*. Beyond this point, the

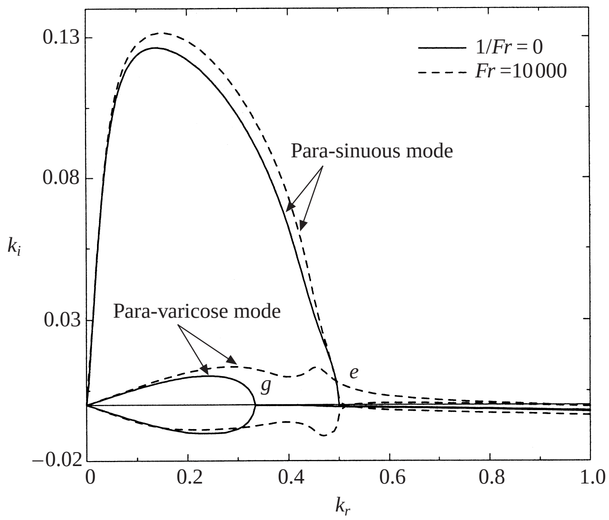

FIGURE 12. The effects of the Froude number on the spatial disturbance growth rate for both modes, $Re = 1000$, $We_i = We_o = 20.0$, $\bar{N}_1 = \bar{N}_3 = 0.018$, $Q_1 = Q_3 = 0.0013$, $r_i = 2$, $r_w = 13$.

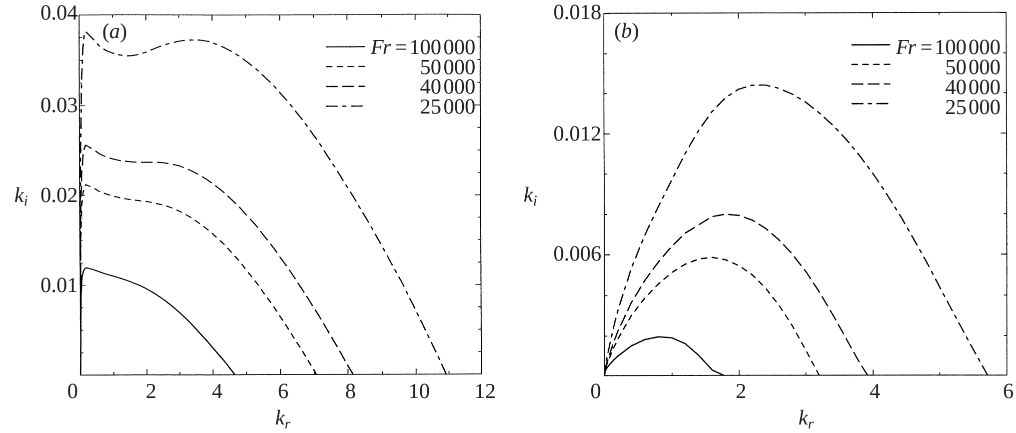

FIGURE 13. The effects of Froude number on the disturbance growth rate, $Re = 2000$, $We_i = We_o = 200\,000$, $\bar{N}_1 = \bar{N}_3 = 0.018$, $Q_1 = Q_3 = 0.0013$, $r_i = 2$, $r_w = 13$. (*a*) Para-sinuous mode. (*b*) Para-varicose mode.

varicose mode dominates over the sinuous mode. However, when gravity is reduced to zero, the dominance of the varicose mode is completely eliminated. Moreover, between the cutoff wavenumbers of the varicose and sinuous modes, even the presence of the varicose mode is completely eliminated. Thus, a sinuous disturbance of a chosen wavelength can be isolated in this range of wavenumbers where the varicose mode is stable, by imparting an external forcing with a frequency corresponding to the chosen wavelength $\lambda = 2\pi h/k_r$. Using the method of Rayleigh, we can estimate the radius of a capsule by equating the volume of the capsule with the volume of the annular jet of length λ from which the capsule is formed. This method of estimation gives the capsule radius R to be $R = [3\pi h(r_i + h)^2/2k_r]^{1/3}$.

It is clear from the results presented up to this point that a successful uniform encapsulation is possible if (i) the process is carried out outside of the absolute

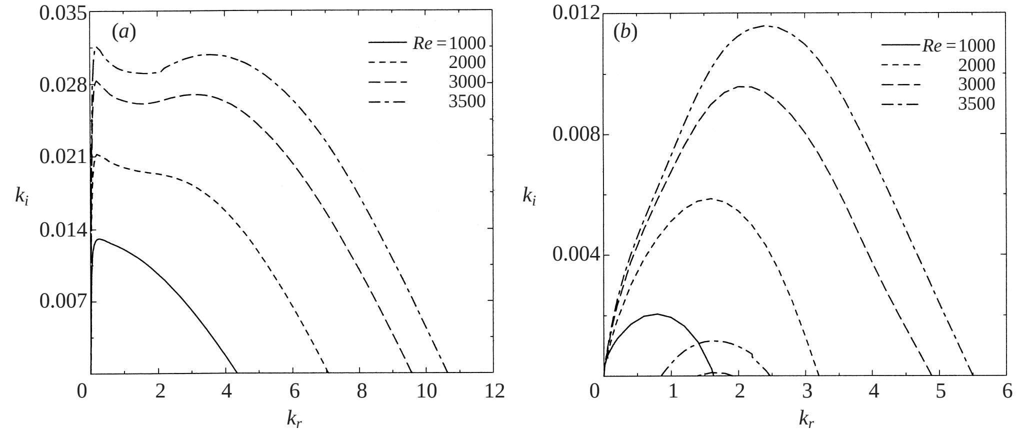

FIGURE 14. The effects of Reynolds number on the disturbance growth rate, $Fr = 50\,000$, $We_i = We_o = 200\,000$, $\bar{N}_1 = \bar{N}_3 = 0.018$, $Q_1 = Q_3 = 0.0013$, $r_i = 2$, $r_w = 13$. (*a*) Para-sinuous mode. (*b*) Para-varicose mode.

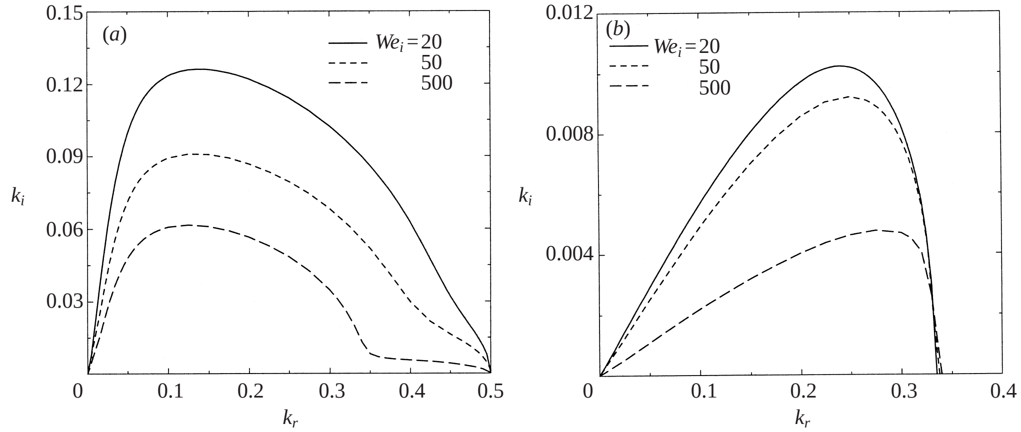

FIGURE 15. The effects of We_i on the disturbance growth rate, $Re = 1000$, $1/Fr = 0.0$, $\bar{N}_1 = \bar{N}_3 = 0.018$, $Q_1 = Q_3 = 0.0013$, $r_i = 2$, $r_w = 13$, $We_o = 20$. (*a*) Para-sinuous mode. (*b*) Para-varicose mode.

instability domain in the parameter space, and (ii) if a monochromatic external excitation is introduced in the wavenumber range where the varicose mode instability is absent but the sinuous mode is convectively unstable. We define the parameter space in which the above two conditions are satisfied to be the encapsulation domain. In the remaining part of this paper, we discuss how the encapsulation domain can be enlarged by varying different flow parameters. Figure 13 shows how the encapsulation domain can be enlarged by reducing the Froude number.

Figure 14 shows that the encapsulation domain widens with increasing *Re*. Figure 15 and 16 show the effect of variations of We_i and We_o, respectively. Encapsulation between $k_r = \frac{1}{3}$ and $\frac{1}{2}$ without varicose mode interference is still possible. Figure 17 shows how the encapsulation domain can be widened by the use of less viscous gas for the outer gas. Figure 18 shows that the encapsulation domain can be enlarged as N_1 is increased with N_3 fixed. Thus, it is easier to encapsulate more viscous fluids.

Figure 19 shows how the encapsulation domain can be enlarged and the difference

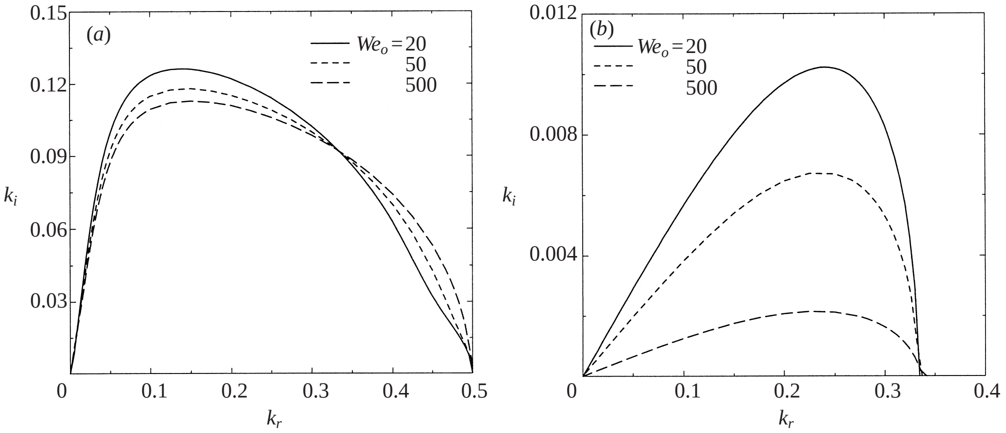

FIGURE 16. The effects of We_o on the disturbance growth rate, $Re = 1000$, $1/Fr = 0.0$, $\bar{N}_1 = \bar{N}_3 = 0.018$, $Q_1 = Q_3 = 0.0013$, $r_i = 2$, $r_w = 13$, $We_o = 20$. (a) Para-sinuous mode. (b) Para-varicose mode.

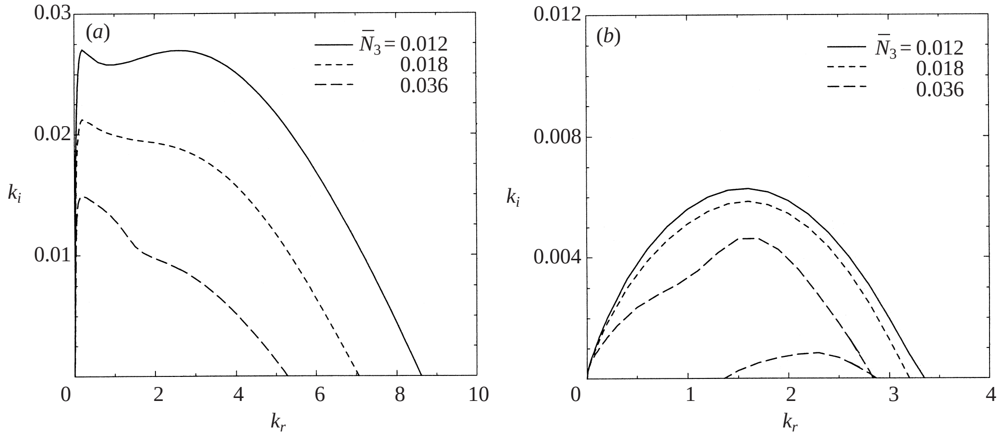

FIGURE 17. The effects of viscosity ratio $\bar{N}_3$, $Re = 2000$, $Fr = 50\,000$, $We_i = We_o = 200\,000$, $Q_1 = Q_3 = 0.0013$, $r_i = 5$, $r_w = 16$, $\bar{N}_1 = 0.018$. (a) Para-sinuous mode. (b) Para-varicose mode.

between the sinuous and varicose mode amplification rates increased by use of a larger pipe radius r_w. Figure 20 shows that it is easier to encapsulate core fluid with smaller diameter relative to the shell thickness, since the configuration has a larger encapsulation domain. As r_w is increased, the amplification rate of the para-sinuous disturbance is increased in figure 19. On the other hand, the para-varicose disturbance amplification is decreased. An increase in the inner radius has the completely opposite effect, as shown in figure 20. It can be shown from the basic flow expression that an increase in r_w is accompanied by a thinning of the shear layer in the outer gas and thickening of the shear layer in the inner gas core. An increase in r_i has the opposite effect on the interfacial shear strain rate. Hence, both figures 19 and 20 are the manifestation of the destabilizing effect of interfacial shear noted earlier by Yih (1967), Hooper & Boyd (1983), Hinch (1984), Kelly *et al.* (1989), Tilley, Davis & Bankoff (1994), Coward & Renardy (1996), and many others.

Figure 21 shows the effect of the gas density variation on the amplification rates. The growth rate of both modes decreases as the gas density is increased. This trend

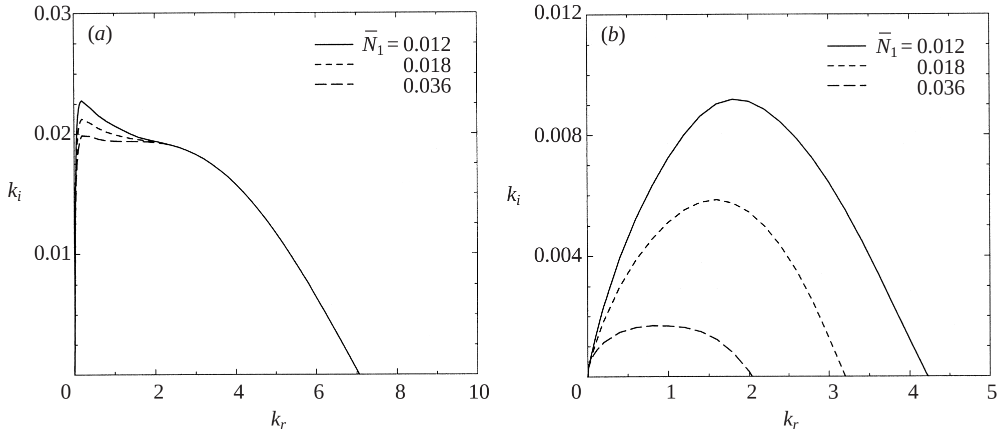

FIGURE 18. The effects of viscosity ratio $\bar{N}_1$, $Re = 2000$, $Fr = 50\,000$, $We_i = We_o = 200\,000$, $Q_1 = Q_3 = 0.0013$, $r_i = 5$, $r_w = 16$, $\bar{N}_3 = 0.018$. (a) Para-sinuous mode. (b) Para-varicose mode.

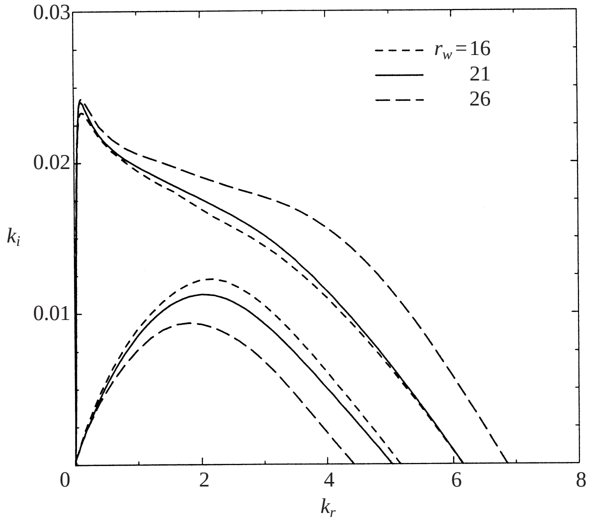

FIGURE 19. The effects of pipe radius on the disturbance growth rate for both mode, $Re = 2000$, $Fr = 50\,000$, $We_i = We_o = 200\,000$, $\bar{N}_1 = \bar{N}_3 = 0.018$, $Q_1 = Q_3 = 0.0013$, $r_i = 10$. The upper three curves are the para-sinuous mode; the lower three curves are the para-varicose mode.

is opposite to that found by Shen & Li (1996) who neglected the effects of the gas viscosity. The trend of the effect cannot be reversed by reducing $\bar{N}_1$ and $\bar{N}_3$. In fact, when N_1 and N_3 instead of $\bar{N}_1$ and $\bar{N}_3$ are fixed so that the effect of density is decoupled from that of the viscosity, the same trend remains. The growth rate of the sinuous mode remains one order of magnitude larger than that of the varicose mode even when the gas density is increased by 100 times. Meanwhile, the amplification rate of the varicose mode is hardly changed. When the density of the outer gas is fixed, the amplification rates of both modes increase with the core gas density, although more dramatically for the varicose mode, as shown in figure 22. As the core gas density increases, the encapsulation domain becomes narrower. Thus, a wider range of drop sizes is possible for lighter core fluids. On the other hand, for a given Q_1, as shown in figure 23, the encapsulation domain increases with increasing Q_3, and hence the gas

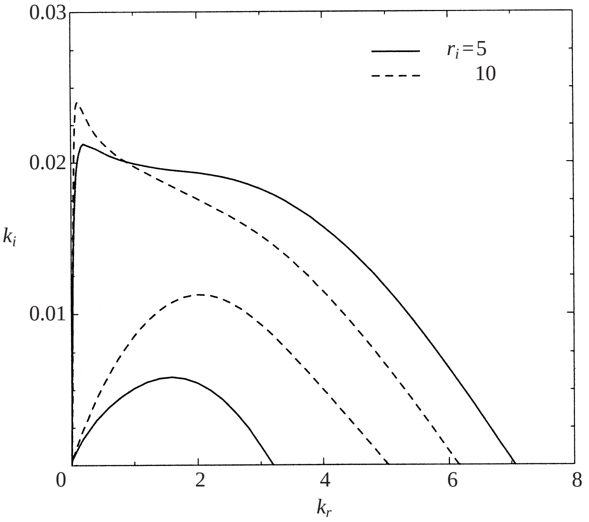

FIGURE 20. The effects of curvature on the disturbance growth rate for both modes, Re = 2000, Fr = 50 000, We_i = We_o = 200 000, $\bar{N}_1$ = $\bar{N}_3$ = 0.018, Q_1 = Q_3 = 0.0013, r_i = 16. The upper two curves are the sinuous mode; the lower two curves are the varicose mode.

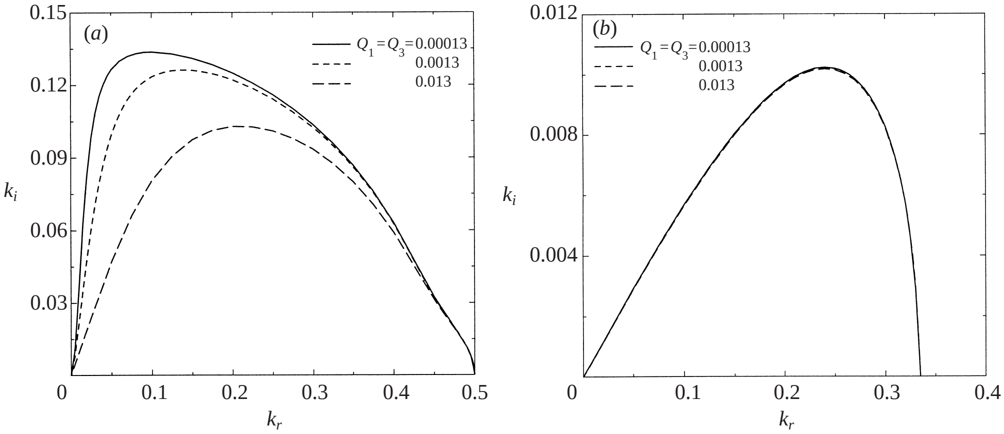

FIGURE 21. The effects of density ratio on the disturbance growth rate, Re = 1000, $1/Fr$ = 0.0, We_i = We_o = 20.0, $\bar{N}_1$ = $\bar{N}_3$ = 0.018, r_i = 2, r_w = 13. (a) Para-sinuous mode. (b) Para-varicose mode.

inertial force outside the annular shell can be promoted to increase the possible size range.

5. Conclusions

The instability of an annular liquid shell with respect to spatio-temporal disturbances is investigated. The annulus is inherently unstable. It is susceptible to unstable para-sinuous and para-varicose modes of convective instability. The amplification rate of the para-sinuous mode is generally much larger. In a certain parameter space the sinuous mode disturbance may cause the annulus to become absolutely unstable. The transition Weber number below which the annulus is absolutely unstable and above

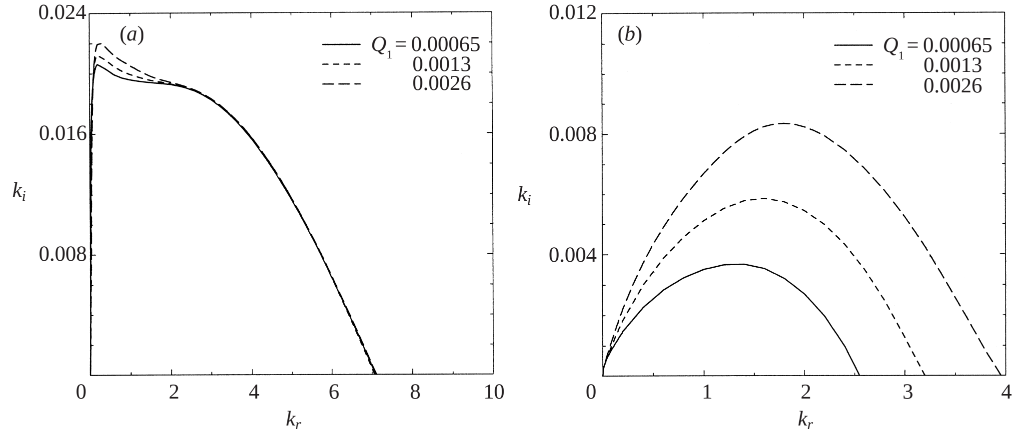

FIGURE 22. The effects of density ratio Q_1, $Re = 2000$, $Fr = 50\,000$, $We_i = We_o = 200\,000$, $\bar{N}_1 = \bar{N}_3 = 0.018$, $r_i = 5$, $r_w = 16$, $Q_3 = 0.0013$. (*a*) Para-sinuous mode. (*b*) Para-varicose mode.

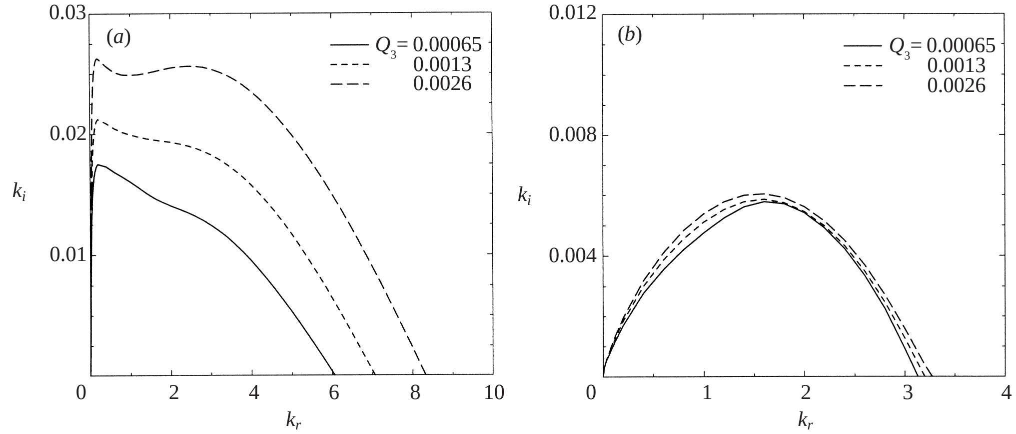

FIGURE 23. The effects of density ratio Q_3, $Re = 2000$, $Fr = 50\,000$, $We_i = We_o = 200\,000$, $\bar{N}_1 = \bar{N}_3 = 0.018$, $r_i = 5$, $r_w = 16$, $Q_1 = 0.0013$. (*a*) Para-sinuous mode. (*b*) Para-varicose mode.

which the flow is convectively unstable is obtained as a function of the Reynolds number, with the rest of the flow parameters held constant. It is shown that a successful encapsulation is possible if the process is carried out outside the parameter space of absolute instability which causes the disturbance to propagate upstream to interrupt the continuous process. An excessive increase in interfacial tension, in the hope of obtaining larger capsules, may lead to an interruption of the process by entering into the parameter space of absolute instability. The convectively unstable sinuous mode must be promoted and the varicose mode suppressed for a possible encapsulation of a core material inside a uniform shell. The encapsulation process is impossible in certain unfavourable parameter spaces in a narrow band of wavenumber in which varicose mode instability dominates the sinuous mode. However, this range of wavenumbers can be eliminated by proper choices of flow parameters, by reducing the level of gravity, for example. There are 10 relevant flow parameters. It is shown how these parameters may be varied to create a condition under which the varicose mode is stable, but the sinuous mode is convectively unstable in a range of wavenumbers. In this range, a monochromatic external forcing may be applied to amplify a selected sinuous mode disturbance to facilitate production of capsules of uniform size and shell thickness.

It is shown that the capillary force stabilizes sinuous as well as varicose mode disturbances of wavelength longer than certain transition wavelengths, but stabilizes relatively short wavelength disturbances. The transitionwave number depends on the flow parameters. Yet the short wavelength disturbances may remain convectively unstable, and therefore their instability is caused by factors other than capillary force. These factors include interfacial pressure and shear fluctuations, Reynolds stresses in the three phase flows, viscous energy dissipation in the three fluids, and the work done by the pressure and viscous stress fluctuation along the flow direction. The quantitative relative importance of these factors can be determined only after a comprehensive energy budget is obtained for a wide range of flow parameters along the line of Lin & Chen (1998) who elucidated the physical mechanism for the case of a simple jet based on an energy consideration. In depth explanation of physical mechanisms involved in absolute and convective instability will be reported together with experimental results in the near future. The possible domains of encapsulation illustrated in this paper will have to be ascertained in the parameter spaces which are actually encountered in the experiments. Extensions of the present analysis to the problems of micro- and nano-encapsulations will find many applications in medical and biological sciences (Benita 1996). It should be pointed out that the present theory predicts the favourable conditions for the initiation of the encapsulation process. The description of the final stage of capsule formation requires a full nonlinear theory.

Appendix. The Orr–Somerfeld system in the Chebyshev space

The derivatives in the Orr–Sommerfeld equation (14) can be transformed into the Chebyshev space defined by (23) using the relations

$$\frac{\mathrm{d}}{\mathrm{d}r} = \frac{\mathrm{d}y}{\mathrm{d}r}\frac{\mathrm{d}}{\mathrm{d}y} = a_j\frac{\mathrm{d}}{\mathrm{d}y} \quad \text{and} \quad \frac{\mathrm{d}^p}{\mathrm{d}r^p} = a_j^p\frac{\mathrm{d}^p}{\mathrm{d}y^p} \quad (j = 1, 2, 3). \tag{A 1}$$

Hence, the transformed Orr–Sommerfeld equation in y remains the same except that the pth derivative in r in (14) must be replaced by (A 1). The same modification must be made in the boundary conditions. Upon substitution of (25) into (14), we must evaluate the derivatives of the cardinal function $h_{jn}(y)$ at the collocation points. Let $\boldsymbol{D}_j^p$ representing the matrix whose elements $d_{j,mn}^p$ are defined by

$$d_{j,mn}^p = \frac{\mathrm{d}^p h_{jn}}{\mathrm{d}y^p}\Big|_{y=y_{j,m}}. \tag{A 2}$$

The matrix $\boldsymbol{D}_j^0$ is a unit matrix and the elements of matrix $\boldsymbol{D}_j^1$ are given by (Boyd 1989)

$$\begin{aligned}
&d_{j,00}^1 = \tfrac{1}{6}(2M_j^2 + 1), \quad d_{j,M_jM_j} = -\tfrac{1}{6}(2M_j^2 + 1),\\
&d_{j,mn}^1 = \frac{-y_{jm}}{(1 - y_{jm}^2)} \quad \text{for} \quad m = n, \quad 1 \leqslant m \leqslant M_j,\\
&d_{j,mn}^1 = \frac{C_m(-1)^{m+n}}{C_n(y_{jm} - y_{jn})} \quad \text{for} \quad m \neq n, \quad 0 \leqslant m, \quad n \leqslant M_j.
\end{aligned}$$

Matrices $\boldsymbol{D}_j^2$, $\boldsymbol{D}_j^3$ and $\boldsymbol{D}_j^4$ are easily obtained by simple matrix multiplication

$$\boldsymbol{D}_j^2 = \boldsymbol{D}_j^1\boldsymbol{D}_j^1, \quad \boldsymbol{D}_j^3 = \boldsymbol{D}_j^1\boldsymbol{D}_j^2, \quad \boldsymbol{D}_j^4 = \boldsymbol{D}_j^2\boldsymbol{D}_j^2. \tag{A 3}$$

The Orr–Sommerfeld equation evaluated at collocation points are

$$\begin{aligned}&\left\{a_j^4 d_{j,mn}^4-\frac{2}{r_{j,m}} a_j^3 d_{j,mn}^3+\left[\left(\frac{3}{r_{j,m}^2}-2k^2\right)-\frac{v_j}{v_2 Re}\mathrm{i}k\bar{w}_{j,m}\right]^2 a_j^2 d_{j,mn}^2\right.\\&\quad+\left[\frac{1}{r_{j,m}}\left(-\frac{3}{r_{j,m}^2}+2k^2\right)+\frac{\mathrm{i}kv_j\overline{w_{j,m}}}{v_2 Re}\right] a_j d_{j,mn}^1\\&\quad\left.+\left[\mathrm{i}k^4+\mathrm{i}k^3\bar{w}_{j,m}+\frac{\mathrm{i}kv_j}{v_2 Re}\left(\frac{\bar{w}'_{j,m}}{r_{j,m}}-\bar{w}''_{j,m}\right)\right] d_{j,mn}^0\right\}\phi_{j,n}\\&\quad=\omega\left\{a_j^2 d_{j,mn}^2-\frac{1}{r_{j,m}} a_j d_{j,mn}^1-k^2 d_{j,mn}^0\right\}\phi_{j,n}\quad(m=0,1,2,\ldots,M_j,\quad j=1,2,3),\end{aligned} \tag{A 4}$$

where

$$\phi_{j,n}=\phi_j(y_{j,n}),\quad r_{j,m}=a_j y_{j,m}+b_j,$$

$$\bar{w}_{j,m}=\bar{w}_j(r_{j,m}),\quad \bar{w}'_{j,m}=\left.\frac{\mathrm{d}w_j(r)}{\mathrm{d}r}\right|_{r=r_{j,m}},\quad \bar{w}''_{j,m}+\left.\frac{\mathrm{d}^2\bar{w}_j(r)}{\mathrm{d}r^2}\right|_{r=r_{j,m}}.$$

The boundary condition (15)–(22) can be written as

$$d_{3,0n}^0\phi_{3,n}=0. \tag{A 5}$$

$$a_3 d_{3,0n}^1\phi_{3,n}=0. \tag{A 6}$$

$$d_{1,0n}^0\phi_{1,n}-d_{2,0n}^0\phi_{2,n}=0. \tag{A 7}$$

$$d_{3,M_3n}^0\phi_{3,n}-d_{2,M_2n}^0\phi_{2,n}=0. \tag{A 8}$$

$$\frac{1}{r_{1,0}}(a_1 d_{1,0n}^1\phi_{1,n}-a_2 d_{2,0n}^1\phi_{2,n})-(\bar{w}'_{1,0}-\bar{w}'_{2,0})\xi_i=0. \tag{A 9}$$

$$\frac{1}{r_{3,M_3}}(a_3 d_{3,M_3n}^1\phi_{3,n}-a_2 d_{2,M_2n}^1\phi_{2,n})-(\bar{w}'_{3,M_3}-\bar{w}'_{2,M_2})\xi_o=0. \tag{A 10}$$

$$\frac{\mathrm{i}k}{r_{1,0}}(d_{1,00}^0\phi_{1,n}+\bar{w}_{1,0})\xi_o=\omega\xi_o. \tag{A 11}$$

$$\frac{\mathrm{i}k}{r_{3,M_3}}d_{3,M_3n}^0\phi_{3,n}+\bar{w}_{3,M_3})\xi_o=\omega\xi_o. \tag{A 12}$$

$$\begin{aligned}&\bar{N}_1\left(a_1^2 d_{1,0n}^2-\frac{1}{r_{1,0}}a_1^1 d_{1,0n}^1+k^2 d_{1,0n}^0\right)\phi_{1,n}\\&\quad-\left(a_2^2 d_{2,0n}^2-\frac{1}{r_{1,0}}a_2^1 d_{2,0n}^1+k^2 d_{2,0n}^0\right)\phi_{2,n}-(\bar{N}_1\bar{w}''_{1,0}-\bar{N}_2\bar{w}''_{2,0})\xi_i=0.\end{aligned} \tag{A 13}$$

$$\begin{aligned}&\bar{N}_3\left(a_3^2 d_{3,M_3n}^2-\frac{1}{r_{3,M_3}}a_3^1 d_{3,M_3n}^1+k^2 d_{3,M_3n}^0\right)\phi_{3,n}\\&\quad-\left(a_2^2 d_{2,0n}^2-\frac{1}{r_{3,M_3}}a_2^1 d_{2,M_2n}^1+k^2 d_{2,M_2n}^0\right)\phi_{2,n}-(N_3\bar{w}''_{3,M_3}-N_2\bar{w}''_{2,M_2})\xi_o=0.\end{aligned} \tag{A 14}$$

$$\begin{aligned}
&\Bigg\{\frac{\bar{N}_1}{Re}\left(a_1^3 d_{1,0n}^3 - \frac{1}{r_{1,0}} a_1^2 d_{1,0n}^2\right) - \left[\frac{\bar{N}_1}{Re}\left(\frac{1}{r_{1,0}^2} - 3k^2\right) + \mathrm{i}kQ_1\bar{w}_{1,0}\right] a_1^1 d_{1,0n}^1 \\
&\quad + \left(\frac{\bar{N}_1}{Re}\frac{2k^2}{r_{1,0}} + \mathrm{i}k\bar{w}'_{1,0}\right) d_{1,0n}^0\Bigg\}\phi_{1,n} - \Bigg\{\frac{1}{Re}\left(a_2^3 d_{2,0n}^3 - \frac{1}{r_{1,0}} a_2^1 d_{2,0n}^2\right) \\
&\quad - \left[\frac{1}{Re}\left(\frac{1}{r_{1,0}^2} - 3k^2\right) + \mathrm{i}k\bar{w}_{2,0}\right] a_2^1 d_{2,0n}^1 + \left(\frac{1}{Re}\frac{2k^2}{r_{1,0}} + \mathrm{i}k\bar{w}'_{2,0}\right) d_{2,0n}^0\Bigg\}\phi_{2,n} \\
&\quad + \mathrm{i}kWe_i^{-1}\left(\frac{1}{r_{1,0}} - r_{1,0}k^2\right)\xi_i = \omega(Q_1 a_1 d_{1,0n}^1 \phi_{1,n} - a_2 d_{2,0n}^1 \phi_{2,n}).
\end{aligned} \tag{A 15}$$

$$\begin{aligned}
&\Bigg\{\frac{1}{Re}\left(a_2^3 d_{2,M_2n}^3 - \frac{1}{r_{3,0}} a_2^2 d_{2,M_2n}^2\right) - \left[\frac{1}{Re}\left(\frac{1}{r_{3,M_3}^2} - 3k^2\right) + \mathrm{i}kQ_2\bar{w}_{2,M_2}\right] a_2^1 d_{2,M_2n}^1 \\
&\quad + \left(\frac{1}{Re}\frac{2k^2}{r_{3,M_3}} + \mathrm{i}k\bar{w}'_{2,M_2n}\right) d_{2,M_2n}^2\Bigg\}\phi_{2,n} - \Bigg\{\frac{\bar{N}_3}{Re}\left(a_3^3 d_{3,M_3n}^3 - \frac{1}{r_{3,M_3}} a_3^2 d_{3,M_3n}^2\right) \\
&\quad - \left[\frac{\bar{N}_3}{Re}\left(\frac{1}{r_{3,M_3}^2} - 3k^2\right) + \mathrm{i}kQ_3\bar{w}_{3,M_3}\right] a_3^1 d_{3,M_3n}^1 \\
&\quad + \left(\frac{\bar{N}_3}{Re}\frac{2k^2}{r_{3,M_3}} + \mathrm{i}k\bar{w}'_{3,M_3}\right) d_{3,M_3n}^0\Bigg\}\phi_{3,n} \\
&\quad + \mathrm{i}kWe_o^{-1}\left(\frac{1}{r_{3,M_3}} - r_{3,M_3}k^2\right)\xi_o = \omega(a_2 d_{2,M_2n}^1 \phi_{2,n} - Q_3 a_3 d_{3,M_3n}^1 \phi_{3,n}).
\end{aligned} \tag{A 16}$$

$$d_{1,M_1n}^0 \phi_{1,n} = 0. \tag{A 17}$$

$$a_1 d_{1,M_1n}^1 \phi_{1,n} = 0. \tag{A 18}$$

Equations (A 4)–(A 18) constitute a system of $(M_1 + M_2 + M_3 + 17)$ algebraic equations. The $(M_1 + M_2 + M_3 + 5)$ unknown vector components are $\phi_{1,0}, \ldots, \phi_{1,M_1}$, $\phi_{2,0}$, $\phi_{2,1}, \ldots, \phi_{2,M_2}$, $\phi_{3,0}$, $\phi_{3,1}, \ldots, \phi_{3,M_3}$, ξ_i and ξ_o. Equation (A 4) comes from three 4th-order ordinary differential equations. Each of these equations, results in $M_j + 1$ equations only $M_j - 3$ of which are independent. Removing 4 equations from each set of governing equations, and adding 14 boundary conditions, we obtain our final system. We remove equations with $m = 0, 1, M_j - 1, M_j$ $(j = 1, 2, 3)$ in (A 4). This is the so-called Lanczos method (1958). The elements of the $\boldsymbol{B}$ and $\boldsymbol{A}$ matrix in (26) can be read off from the coefficients of the unknown vector components. The $\boldsymbol{B}$ matrix involves only terms with ω.

REFERENCES

Baird, M. H. I. & Davidson, J. F. 1962 Annular jets – I: Fluid Mechanics. *Chem. Engng Sci.* **17**, 467–472.

Benita, S. 1996 *Microencapsulation.* Marcel Dekker, New York.

Bers, A. 1983 *Handbook of Plasma Physics*, vol. 1, pp. 452–516. North Holland.

Boyd, J. P. 1989 *Chebyshev and Fourier Spectral Method.* Springer.

Briggs, R. J. 1964 *Electron Stream Interaction with Plasma.* MIT Press.

Coward, A. V. & Renardy, Y. Y. 1996 Small amplitude oscillatory forcing on two-layer plane channel flow. *J. Fluid Mech.* **334**, 87–109.

Crapper, G. D., Dombowski, N. & Pyott, G. A. D. 1975 Kelvin–Helmholtz wave growth on cylindrical sheets. *J. Fluid Mech.* **68**, 497–502.

Davey, A. & Drazin, P. G. 1969 Stability of Poiseuille flow in a pipe. *J. Fluid Mech.* **36**, 209–218.

Drazin, P. G. & Reid, W. H. 1985 *Hydrodynamic Stability*. Cambridge University Press.

Hertz, C. H. & Hermanrud, B. 1983 A liquid compound jet. *J. Fluid Mech.* **131**, 271–287.

Hinch, E. J. 1984 A note on the mechanism of the instability at the interface between two shearing fluids. *J. Fluid Mech.* **144**, 463–468.

Hooper, A. P. & Boyd, W. G. C. 1983 Shear flow instability at the interface between two viscous fluids. *J. Fluid Mech.* **128**, 507–528.

Hu, H. H. & Joseph, D. D. 1989 Lubricated pipelining: stability of core–annular flow. Part 2. *J. Fluid Mech.* **205**, 359–396.

Keller, J. B., Rubinow, S. I. & Tu, Y. O. 1973 Spatial instability of a jet. *Phys. Fluids* **16**, 2052–2055.

Kelly, R. E., Goussis, D. A., Lin, S. P. & Hsu, F. K. 1989 The mechanism of surface wave instability in film flow down an inclined plane. *Phys. Fluids* A **1**, 819–828.

Kendall, J. M. 1986 Experiments on annular liquid jet instability and on the formation of liquid shells. *Phys. Fluids* **29**, 2086–2094.

Lanczos, C. 1956 *Applied Analysis*. Prentice Hall.

Lee, J. G. & Chen, L. D. 1991 Linear stability analysis of gas–liquid interface. *AIAA J.* **29**, 1589–1595.

Lee, C. P. & Wang, T. G. 1989 The theoretical model for the annular jet instability – revisited. *Phys. Fluids* A **1**, 967–964.

Lin, S. P. & Chen, J. N. 1998 roles played by the interfacial shear in the instability mechanism of a viscous liquid jet surrounded by a viscous gas in a pipe. *J. Fluid Mech.* **376**, 37–51.

Meyer, J. & Weihs, D. 1987 Capillary instability of an annular liquid jet. *J. Fluid Mech.* **179**, 531–545.

O'Donnell, B., Chen, J. N. & Lin, S. P. 2001 Transition from convective to absolute instability in a pipe. *Phys. Fluids* **13**, 2732–2734.

Sanz, A. & Meseguer, J. 1985 One-dimensional linear analysis of the compound jet. *J. Fluid Mech.* **159**, 55–68.

Shen, J. & Li, X. 1996 Instability of an annular viscous liquid jet. *Acta Mech.* **114**, 167–183.

Tilley, B. S., Davis, S. H. & Bankoff, S. G. 1994 Linear stability of superposed fluids in an inclined channel. *Phys. Fluids* **6**, 3906–3922.

Yih, C. S. 1967 Instability due to viscosity stratification. *J. Fluid Mech.* **67**, 337–352.